Materials & Design 250 (2025) 113569

Contents lists available at ScienceDirect

Materials & Design

journal homepage: www.elsevier.com/locate/matdes

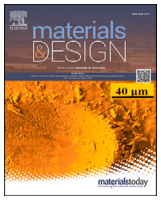

Multi-objective parametric optimisation of architected hexagonal honeycomb with stepped struts

F.I. Azam [a], P.J. Tan [a], F. Bosi [a,b,*]

[a] Department of Mechanical Engineering, University College London, UK
[b] Department of Innovative Technologies, University of Applied Sciences and Arts of Southern Switzerland, Switzerland

ARTICLE INFO

Keywords:
Mechanical metamaterials
Lattices
Optimisation
Auxetic materials
Additive manufacturing

ABSTRACT

Recent advances in small-scale fabrication enable the creation of architected metamaterials with tailored mechanical properties by manipulating their structures at the micro and nanoscale. In this study, the shape of 2D hexagonal honeycombs is modified by redistributing solid material to create stepped struts with two thicknesses. Analytical expressions are derived to show the effect of the geometric parameters on the unit cell stiffness, buckling and plastic strengths. An analytical multi-objective optimisation is performed to find the design parameters that simultaneously maximise stiffness and strength in the range of relative densities of cellular solids. Theoretical results show that a stepped strut can simultaneously enhance the stiffness of the uniform honeycomb by 36.3% and the plastic strength by 36.5%. For low relative densities, redistributing material does not significantly enhance the buckling strength of the uniform hexagonal architecture, but a stiffness gain of 29.1% is observed. Failure maps are provided to assess the influence of relative density and design parameters on the lattice failure mode. The analytical results are validated by finite element modelling and experiments, showing excellent agreement. Therefore, the study demonstrates a parametric shape optimisation approach, which can be extended to enhance the performance of other 2D and 3D mechanical metamaterials.

1. Introduction

Architected materials are engineered solids encompassing a combination of different constituents or rationally designed architecture at smaller scales to achieve unique properties that cannot be found in standard materials [1,2]. In particular, mechanical metamaterials are those designed to achieve specific mechanical properties through periodic or quasi-periodic architectures. This has led to the creation of materials exhibiting novel quasi-static and dynamic properties [3], such as negative Poisson's ratio [4], negative stiffness [5,6], superelasticity [7], and adaptive responses [8–11]. Some notable advances in the field have been possible due to the development of micro and nano-fabrication techniques, such as 3D printing, that enable the fabrication of complex architectures with precise control over their geometry, thus facilitating the manufacturing of materials with tailored properties [12–14].

Within this framework, honeycombs represent a class of two-dimensional structured materials studied in the past few decades because of their favourable mechanical properties and manufacturability [15]. Analytical, numerical, and experimental approaches have been used to determine the elastic constants and plastic strength of regular honeycombs, which are mainly influenced by four factors: (i) material properties, (ii) unit cell architecture, (iii) relative density and (iv) geometrical features of the cell wall. Gibson and Ashby [16] is the most commonly used reference to analytically predict the mechanical properties of honeycombs under uniaxial, biaxial, and shear loading through beam analysis of a representative strut with constant cross-section. Such analytical formulation can also be extended to include honeycombs with double-wall thicknesses, as long as the thickness of cell walls remains uniform [17,18]. Alternative analytical or semi-analytical methods have been proposed to estimate the mechanical properties of periodic lattices, including micromechanical models [19], energy approaches [20] and homogenization techniques [21]. To complement those, numerical and experimental methods have also been widely used to predict and validate the mechanical response of lattices. Depending on the lattice's relative density, finite element models can use different element types, including beam, shell and solid elements, that offer a trade-off between accuracy and computational time [22]. Several experimental campaigns have also been performed to measure the static [23,24] and dynamic [25] effective properties of honeycombs following standardised methods, such as ASTM C365 and C273.

* Corresponding author at: Department of Mechanical Engineering, University College London, UK.
E-mail addresses: f.bosi@ucl.ac.uk, federico.bosi@supsi.ch (F. Bosi).

https://doi.org/10.1016/j.matdes.2024.113569
Received 9 November 2024; Received in revised form 10 December 2024; Accepted 24 December 2024
Available online 9 January 2025

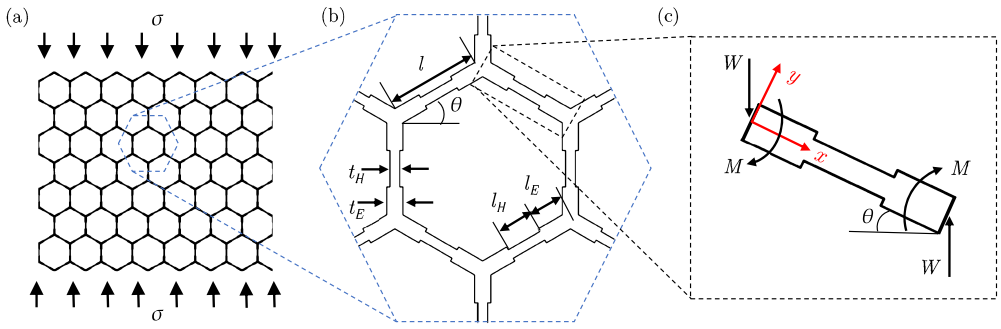

Fig. 1. (a) Hexagonal lattice subjected to remote a uniaxial compressive stress σ, (b) its representative unit cell for the stepped strut configuration and (c) its representative strut free body diagram illustrating the forces and bending moments.

Most studies assessing the mechanical behaviour of lattices assume the uniform thickness of the cell walls and evenly distributed solid material [16,15]. However, the morphology of fabricated lattice structures is imperfect and can contain irregularities, non-uniform cell wall thickness, and uneven material distribution, especially at the joints [26,27]. These imperfections are often influenced by manufacturing methods and processing, thus affecting the properties of honeycombs. However, they can also be rationally introduced by designers to obtain tailored functionalities and properties. Pioneering studies by Simone and Gibson [28] and Zhu et al. [29] assessed the effect of solid distribution along the cell wall on the variation of 2D and 3D lattices responses, reporting that the redistribution of material towards joints can increase the stiffness and plastic strength up to an extent before a decrease in mechanical properties is observed. Following these works, Storm et al. [30] showed, through finite element beam and solid models, that a non-uniform cross-section of ligaments can increase the stiffness and strength of open-cell foams with tetrakaidecahedral and kelvin unit cells, respectively. The investigation of solid redistribution in kelvin unit cells was complemented by the work of Zargarian et al. [31], who performed a numerical and experimental investigation that showed how the elastic modulus of the lattice tends to increase with a shift in material away from the edges and towards vertices, until a critical point after which it starts to decrease. Focussing on honeycombs, the theoretical study of Simone and Gibson [28] showed the improved in-plane uniaxial stiffness and plastic strength achievable for certain configurations of 2D hexagonal lattices with plateau borders, where the material is moved from cell edges to vertices, which are characterised by curved profile defined by one geometric parameter, i.e. the constant radius. Later, Chuang and Huang [32] and Yang and Huang [33] analysed the uniaxial and biaxial buckling strength of honeycomb with the same topology of plateau borders, using semi-analytical and numerical approaches, respectively. In both cases, a limited increase in buckling strength was observed as a result of such predefined material redistribution. More recently, Zhang et al. [34] analytically and experimentally studied the variation in elastic modulus in honeycomb with stepped struts, where the variation of thickness along the cell walls is geometrically described by two parameters. They found a configuration that guarantees a theoretical increase of elastic modulus of 37%, as compared to the uniform thickness honeycomb. However, the effect of such stepped thickness distribution on other mechanical properties, such as plastic and buckling strengths, was not considered. In addition to in-plane properties, Lin et al. [35] also showed that the out-of-plane properties of honeycomb are significantly affected by material redistribution along the cell walls.

The aforementioned studies have shown that the redistribution of solid material along the cell walls affects the lattice response. This effect can be utilised to optimise the mechanical properties by tuning the shape of unit cells and is the main inspiration for the presented work. This is even more important than ever due to the development of additive microfabrication techniques, which provide the freedom to alter solid fractions in the cell walls with great accuracy. However, the research work on solid redistribution in hexagonal honeycomb has been limited to certain shapes of the struts, mainly with plateau borders, and to a single property to enhance, without considering a strut shape that simultaneously optimises multiple mechanical properties, such as stiffness and plastic or buckling strengths. Hence, the paper aims at establishing an analytical framework, validated numerically and experimentally, to perform a multi-objective parametric shape optimisation of the strut thickness that simultaneously enhances the uniaxial effective elastic modulus, plastic and buckling strengths. For this purpose, inspired by the work of Zhang et al. [34], a 2D hexagonal honeycomb with stepped struts is selected because its bending-dominated architecture will benefit from solid material distribution along the strut. The work shows the relative density and design parameters-dependent failure maps and identifies a shape profile that, despite the suboptimal stepped configuration, simultaneously increases the effective stiffness and plastic strength of the uniform lattice (i.e. with constant strut thickness) by 36.3% and 36.5%, respectively. The paper is organised as follows: Section 2 presents the analytical derivation for the calculation of the stiffness, plastic and buckling strengths of hexagonal honeycomb with stepped strut thickness profiles, showing how the geometric parameters affect the mechanical response and critical relative density, and they can be selected to independently optimise each property. Section 3 shows the multi-objective optimization that enables the selection of the best geometric parameters that simultaneously enhance the stiffness and strength of the strut profile. The analytically derived predictions are validated through finite element simulations and experimental tests, described in Section 4 and Section 5, respectively. The results obtained are presented and discussed in Section 6 and summarised in Section 7.

2. Analytical approach

We consider two-dimensional hexagonal honeycombs subjected to remote uniaxial compression loading σ, whose response can be studied by analysing a hexagonal unit cell subjected to periodic boundary conditions, Fig. 1(a,b). The strategy considered to redistribute materials along the cell wall consists of a stepwise transition in thickness, thus resulting in a lattice termed as *stepped strut* honeycomb and denoted by a subscript SS in the following. The stepped strut hexagonal honeycomb is created by moving the solid material of the regular hexagonal honeycomb from the middle of the strut towards the node, as shown in Fig. 1(c). This creates two cross-sections in a strut, the middle section, and the end section, with different lengths and thicknesses. The middle section is denoted by a subscript H, with its length and thickness defined by l_H and t_H, respectively. The end section is denoted by E, with its length and thickness that are l_E and t_E, respectively. The second moments of area for the middle and end sections are denoted as I_H and I_E, respectively. The shape of the stepped strut honeycomb can be parameterised by using two geometric parameters. The first is η, which represents the ratio between the middle and the end section thicknesses

$$\eta = \frac{t_H}{t_E}, \tag{1}$$

where $0 < \eta \leq 1$ and $\eta = 1$ gives the uniform thickness honeycomb. The second geometric parameter is ξ, which is the ratio between the length of the middle section l_H and the total length of the strut l

$$\xi = \frac{l_H}{l} = \frac{l_H}{l_H + 2l_E}, \tag{2}$$

where $0 \leq \xi \leq 1$ and $\xi = 0$ and $\xi = 1$ represent a strut with uniform thickness.

In the following sections, the stepped strut configuration is analysed to determine its mechanical properties, which will be benchmarked against those of the uniform thickness (or regular) honeycomb to assess the effect of material redistribution on the lattice response. The effective elastic properties of the regular hexagonal honeycomb have been extensively studied in the literature, and the scaling laws to compute the stiffness, plastic strength, and buckling strength are [16]

$$\frac{E_U}{E_s} = \frac{3}{2}\overline{\rho}^3, \qquad \frac{(\sigma_p)_U}{\sigma_{ys}} = \frac{1}{2}\overline{\rho}^2, \qquad \frac{(\sigma_b)_U}{E_s} = 0.143\,\overline{\rho}^3, \tag{3}$$

where E_U, $(\sigma_p)_U$, and $(\sigma_b)_U$ represent the elastic modulus, plastic strength, and buckling strength for the hexagonal lattice with uniform thickness, respectively. These properties depend on the lattice's relative density and the response of the constituent material, assumed elasto-perfectly plastic and characterised by Young's modulus E_s and yield strength σ_{ys}. The first-order approximation of the relative density for regular hexagonal lattice is $\overline{\rho} = (2/\sqrt{3})(t/l)$, which is a function of the strut aspect ratio t/l, where t and l are the strut thickness and length, respectively. The expressions in Eq. (3) can only predict the mechanical properties accurately for low relative densities and low aspect ratio of the strut, often defined by the range of validity of the Euler-Bernoulli (EB) beam theory, when $t/l < 1/15$, above which the axial and shear effects cannot be neglected.

2.1. Stiffness

The stiffness of the stepped honeycomb under uniaxial compression can be calculated using beam theory, following the same procedure employed to obtain the effective elastic modulus of regular honeycomb [16]. The analysis can be performed on a representative inclined strut, as shown in Fig. 1(c), by deriving its strain energy and calculating its deflection via Castigliano's theorem. The full derivation is omitted here because it is given in [34]. From the strut deflection, it is possible to obtain the unit cell's effective strain, and lastly, the stiffness of the stepped strut honeycomb, E_{SS}, can be calculated by dividing the applied effective stress and strain as

$$\frac{E_{SS}}{E_s} = \frac{4}{\sqrt{3}} \frac{1}{\xi^3 + \eta^3 - \xi^3\eta^3} \left(\frac{t_H}{l}\right)^3, \tag{4}$$

showing that the stiffness of a stepped-strut honeycomb depends on the ratio of the thickness of the middle section to strut length, t_H/l, and the two geometric parameters ξ and η. As the analytical formulation is based on Euler Bernoulli's beam theory, the obtained expression is only valid for a low strut aspect ratio, the ratio between the beam thickness t_H and length l, or, equivalently, for low relative densities. It should be noted that if the aspect ratios of the end and middle sections are calculated alone considering their lengths l_E and l_H, they could deviate from the theoretical limit of the Euler Bernoulli beam theory for some combinations of design parameters. Nevertheless, the comparison between the analytical formulation, finite element analysis (FEA) and experiments reported in the following sections shows the robustness of the analytical model and the negligible influence of any potential deviation from the ideal Euler Bernoulli beam for the range of relative densities considered. The stiffness expression of Eq. (4) can also be reported as a scaling law, in terms of the lattice relative density. To this purpose, a relation between the minimum strut aspect ratio t_H/l and relative density $\overline{\rho}$ can be obtained as

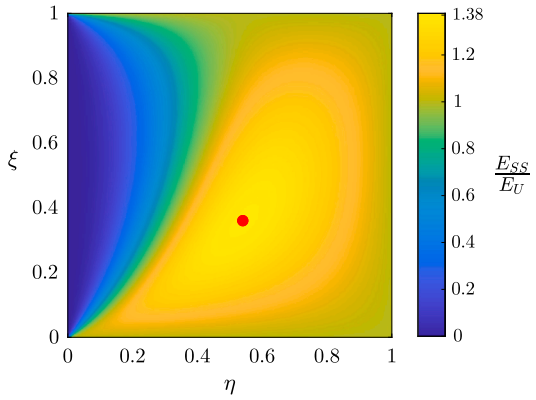

Fig. 2. Contour plot showing the stiffness of stepped strut honeycomb, E_{SS}, normalised by that of the regular honeycomb, E_U, as a function of the design parameters ξ and η. The configuration that maximises the stiffness, highlighted by a red circle, is given by $\xi = 0.36$ and $\eta = 0.54$, for which $E_{SS}/E_U = 1.378$.

$$\overline{\rho} = \frac{\rho_{SS}}{\rho_s} = \frac{2}{\sqrt{3}} \frac{1 - \xi + \xi\eta}{\eta} \frac{t_H}{l}. \tag{5}$$

Therefore, Eq. (4) becomes

$$\frac{E_{SS}}{E_s} = \frac{3}{2} \frac{\eta^3}{(1 - \xi + \xi\eta)^3} \frac{1}{\xi^3 + \eta^3 - \xi^3\eta^3} \overline{\rho}^3. \tag{6}$$

It should be noted that Eq. (6) reduces to Eq. (3) if either $\xi = 0$, $\xi = 1$ or $\eta = 1$, when the strut assumes a uniform thickness.

To ensure a fair comparison, the mass, volume and relative density of the unit cell are kept constant when the material is redistributed, thus satisfying the condition $\rho_{SS} = \rho_U$. A comparative expression between the stepped strut and regular hexagonal lattices can be obtained by imposing equal relative density and normalising the stepped strut stiffness by the regular honeycomb stiffness. The relative density equivalence provides a relationship between the thickness of the uniform honeycomb, t, and that of the stepped strut honeycomb, t_H, through the geometrical parameters η and ξ

$$t_H = t \frac{\eta}{1 - \xi + \xi\eta}. \tag{7}$$

This equation relates the stepped strut's middle thickness t_H to the original uniform strut thickness t, ensuring that the material volume per unit cell remains constant despite the change in geometry. Combining Eqs. (3), (6) and (7) yields the ratio between the stiffnesses of stepped strut and uniform hexagonal lattices

$$\frac{E_{SS}}{E_U} = \frac{1}{\xi^3 + \eta^3 - \xi^3\eta^3} \frac{\eta^3}{(1 - \xi + \xi\eta)^3}, \tag{8}$$

which depends only on the geometric parameters ξ and η and can be plotted to visualise the gain ($E_{SS}/E_U > 1$) or loss ($E_{SS}/E_U < 1$) in stiffness with respect to the regular honeycomb, as shown in Fig. 2. From the plot, it is evident that the ratio of moduli tends to increase when material from the middle section is transferred to the end sections until certain values of ξ and η, after which it starts to decrease. The maximum value of $E_{SS}/E_U = 1.378$ can be obtained for $\xi = 0.36$ and $\eta = 0.54$, which proves that the stiffness of hexagonal lattice can be enhanced by 37.8% by redistributing the material in a stepwise manner, as reported in [34]. The plot also shows the ratio $E_{SS}/E_U = 1$ at $\xi = 0$, $\xi = 1$ and $\eta = 1$, where the thickness of the strut becomes uniform and the stiffness of stepped strut hexagonal lattice, E_{SS}, becomes equal to that of the uniform honeycomb, E_U.

2.2. Plastic strength

The stepped strut has two different cross-sections, H and E, which lead to two different plastic moments, $M_{PH} = \sigma_{ys}\, b t_H^2/4$ and $M_{PE} =$

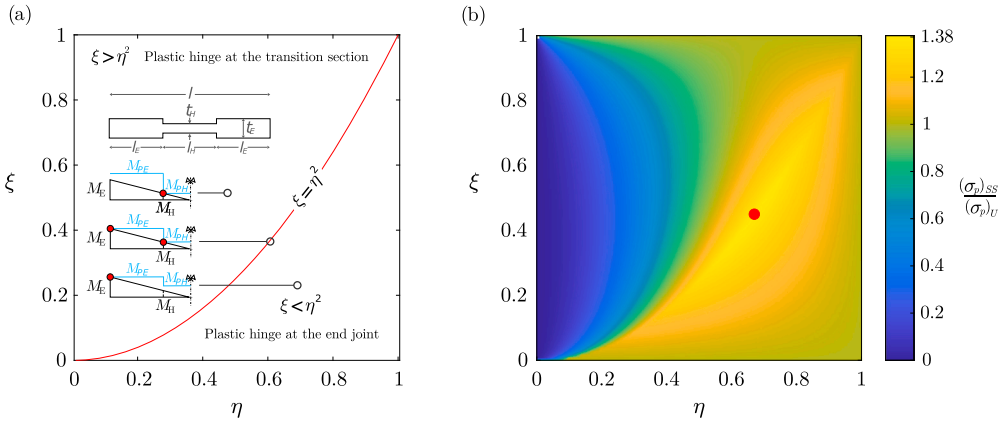

Fig. 3. (a) Location of plastic hinge formation as a function of the design parameters. (b) Contour plot of normalised plastic strength, $(\sigma_p)_{SS}/(\sigma_p)_U$, of stepped strut hexagonal honeycomb as a function of the geometric design parameters ξ and η. The parameters combination maximising the strength value is highlighted with a red circle, given by $\xi = 0.45$ and $\eta = 0.67$, for which $(\sigma_p)_{SS}/(\sigma_p)_U = 1.376$.

$\sigma_{ys}\, b\, t_H^2/(4\eta^2)$. With reference to Fig. 1(c), the bending moment along the strut's longitudinal coordinate is $M(x) = W\cos\theta\,(l/2 - x)$, where $W = \sigma\, b\, l\cos\theta$ and $\theta = \pi/6$. Hence, the bending moment at the node $(x = 0)$ is $M_E = W\, l\cos\theta/2$, while that at the step wise transition section $(x = l_E)$ is $M_H = W\, l\,\xi\cos\theta/2$. When the internal bending moment M equals the plastic moment M_P, a plastic hinge forms at a specific longitudinal coordinate x. Considering the symmetry of the strut, we restrict the attention to $0 \le x \le l/2$. Depending upon the geometric parameters ξ and η and relying on the linear variation of the internal bending moment, we can distinguish three cases, as shown in Fig. 3(a):

(i) The plastic hinge forms at the node when the difference in internal bending moments, M_E and M_H, is greater than the difference in plastic moments, M_{PE} and M_{PH}. This condition writes $M_E - M_H > M_{PE} - M_{PH}$ and occurs when $\xi < \eta^2$. In this case, the plastic strength of the stepped strut honeycomb, $(\sigma_p)_{SS}$, can be determined by equating the internal bending moment and plastic moment at the node, $x = 0$, as

$$M_E = M_{PE} \iff \frac{(\sigma_p)_{SS}}{\sigma_{ys}} = \frac{2}{3}\frac{1}{\eta^2}\left(\frac{t_H}{l}\right)^2 \quad \text{for} \quad \xi < \eta^2 \tag{9}$$

(ii) The plastic hinge forms at the transition section when the difference in internal bending moments, M_E and M_H, is less than the difference in plastic moments in both sections, M_{PE} and M_{PH}. This condition writes $M_E - M_H < M_{PE} - M_{PH}$ and occurs when $\xi > \eta^2$. In this case, the plastic strength of the unit cell can be determined by equating the internal bending moment and plastic moment at the transition section, $x = l_E$, as

$$M_H = M_{PH} \iff \frac{(\sigma_p)_{SS}}{\sigma_{ys}} = \frac{2}{3}\frac{1}{\xi}\left(\frac{t_H}{l}\right)^2 \quad \text{for} \quad \xi > \eta^2 \tag{10}$$

(iii) Plastic hinges form simultaneously at the node, $x = 0$, and at the transition section, $x = l_E$, when the difference in internal bending moments, M_E and M_H, is equal to the difference in plastic moment, M_{PE} and M_{PH}, which occurs when $\xi = \eta^2$. In this particular case, the internal bending moments at both locations are equal to the respective plastic moments. Therefore, both expressions in Eq. (9) and Eq. (10) can predict the plastic behaviour of the stepped strut hexagonal unit cell.

Eq. (9) and Eq. (10) can be expressed in terms of the relative density by making use of Eq. (7), thus providing the scaling law for the plastic strength of stepped strut honeycomb

$$\frac{(\sigma_p)_{SS}}{\sigma_{ys}} = \begin{cases} \dfrac{1}{2}\dfrac{1}{(1-\xi+\xi\eta)^2}\,\overline{\rho}^2, & \text{for} \quad \xi \le \eta^2 \\ \dfrac{1}{2}\dfrac{\eta^2}{\xi(1-\xi+\xi\eta)^2}\,\overline{\rho}^2, & \text{for} \quad \xi > \eta^2. \end{cases} \tag{11}$$

Similar to stiffness, an expression can be derived to quantify the change in plastic strength from regular hexagonal lattices to stepped strut honeycombs. Combining Eq. (3) and Eq. (11), the normalised strength can be obtained as

$$\frac{(\sigma_p)_{SS}}{(\sigma_p)_U} = \begin{cases} \dfrac{1}{(1-\xi+\xi\eta)^2}, & \text{for} \quad \xi \le \eta^2 \\ \dfrac{1}{\xi}\dfrac{\eta^2}{(1-\xi+\xi\eta)^2}, & \text{for} \quad \xi > \eta^2 \end{cases} \tag{12}$$

which only depends on the geometric parameters ξ and η. Eq. (12) can be plotted to visualise the design space that allows an increase of plastic strength with respect to the uniform thickness honeycomb and find the shape that maximises the strength, Fig. 3(b). The plastic strength of the stepped strut hexagonal honeycomb is maximum when $\xi = \eta^2$, i.e. plastic hinges appear at both end and transition sections. The highest value of the strength specific ratio, $(\sigma_p)_{SS}/(\sigma_p)_U = 1.376$, is found for $\xi = 0.45$ and $\eta = 0.67$. This shows a 37.6% increase in plastic strength when material along the cell strut is redistributed in a stepwise manner. It should be noted that the geometric parameters resulting in the maximum strength are different from the ones that guarantee maximum stiffness. Similar to the stiffness plot, $(\sigma_p)_{SS}/(\sigma_p)_U = 1$ at $\xi = 0$, $\xi = 1$ and $\eta = 1$, where the thickness of the strut becomes uniform; thus, the strength of stepped strut honeycomb, $(\sigma_p)_{SS}$, becomes equal to uniform thickness hexagonal lattice, $(\sigma_p)_U$.

2.3. Elastic buckling strength

The buckling strength of the stepped strut honeycomb, $(\sigma_b)_{SS}$, is calculated considering it undergoes elastic instability following the first buckling mode of the regular honeycomb, as shown in Fig. 4(a). This assumption has been validated through finite element simulations, Section 4. Under remote vertical uniaxial stress, the struts aligned along the loading direction might buckle, constrained through the node by the connecting inclined struts, which undergo bending. The first buckling mode of representative struts reported in Fig. 4(a) shows that the top and bottom ends of the vertical strut BD move sideways in opposite directions while also rotating and being constrained by the inclined struts. This suggests that the buckling strut's end joints B and D have a rotational stiffness between a pin joint and a fully clamped joint, modelled as a rotational spring in the following. Hence, employing symmetry

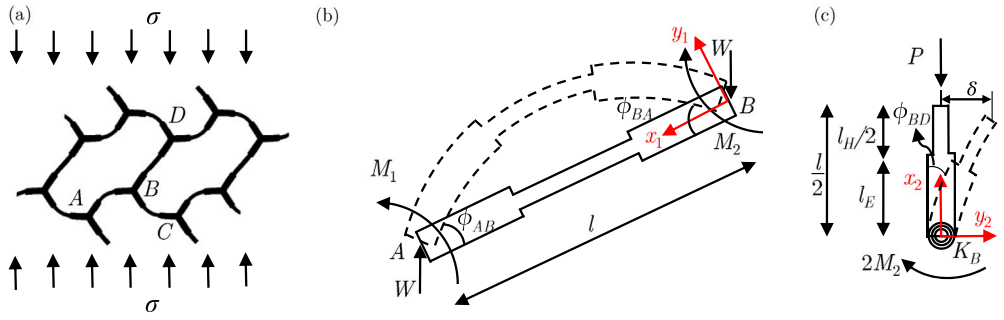

Fig. 4. Stepped strut hexagonal lattice deformation under elastic buckling. (a) First buckling mode of representative cells under uniaxial compression. (b) Deflection and free body diagram of the inclined strut AB undergoing bending. (c) Deflection and free body diagram of the vertical strut BD under buckling triggered by the axial force $P = 2W$; a rotational spring with stiffness K_B is represented to mimic the nodal response, while only half strut is represented because of symmetry.

of the vertical strut B, half of the strut can be modelled as a spring-hinged (node B)-free (midspan) condition, as shown in Fig. 4(c). Before assessing the buckling of the vertical strut BD, the rotational stiffness at node B must be determined by analysing the bending behaviour of the representative inclined strut AB, Fig. 4(b). Redistributing material by varying the geometric parameters ξ and η changes the amount of material at the nodes, resulting in a change of nodal rotational stiffness. Hence, with reference to Fig. 4(a), in the following the buckling analysis is performed by first studying the bending response of the representative inclined struts AB and BC to calculate the rotational stiffness at the node B, which is a function of the geometric parameters. Then, the buckling response of the stepped strut honeycomb is obtained by studying the Eulerian buckling of the representative vertical strut BD using the nodal rotational stiffness from the previous step.

Firstly, the nodal rotational stiffness is determined by isolating and analysing the bending response of strut AB [16], Fig. 4(b). As the strut has varying cross-sections, the beam deflection equation for each section can be written as

$$E_s I_i \frac{d^2 y_1}{dx_1^2} = -M_2 - \frac{M_1 - M_2}{l} x_1, \quad \text{where} \quad i = \begin{cases} E & \text{for } 0 \le x_1 \le l_E,\ (l_E + l_H) < x_1 \le l \\ H & \text{for } l_E < x_1 < (l_E + l_H). \end{cases} \tag{13}$$

The above equation can be integrated to obtain the rotation field $\phi = dy_1/dx_1 = y_1'$ by defining ϕ_{BA} and ϕ_{AB} as the rotations at $x_1 = 0$ and $x_1 = l$, respectively. Furthermore, rotational continuity is set at the step-wise transition by prescribing $y_1'(x_1 = l_E^+) = y_1'(x_1 = l_E^-)$. Imposing the boundary conditions, the constants of integration are obtained, and the rotation at the end B of the strut AB becomes

$$\phi_{BA} = M_2 \left(\frac{l_E}{E_s I_E} - \frac{l_E}{E_s I_H} + \frac{l}{2 E_s I_H} \right). \tag{14}$$

The rotation of each strut converging into node B is the same because of nodal continuity, hence $\phi_{BA} = \phi_{BC} = \phi_{BD}$. Moreover, considering the symmetry between the struts AB and BC and the moment equilibrium at the node B ($M_{BD} = 2M_2$), it is possible to compute the rotational stiffness K_B of the strut BD at node B as

$$K_B = \frac{M_{BD}}{\phi_{BD}} = \frac{2}{\left(\frac{l_E}{E_s I_E} - \frac{l_E}{E_s I_H} + \frac{l}{2 E_s I_H} \right)}. \tag{15}$$

Secondly, half of the strut BD is considered for buckling analysis due to symmetry, as shown in Fig. 4(c). The deflection equations for the two different cross-sections subjected to an axial force $P = 2W$ are given as

$$E_s I_i \frac{d^2 y_2}{dx_2^2} = P(\delta - y_2), \quad \text{where} \quad i = \begin{cases} E & \text{for } 0 \le x_2 \le l_E \\ H & \text{for } l_E < x_2 \le l/2 \end{cases}. \tag{16}$$

Defining $\lambda_i = \sqrt{P/(E_s I_i)}$ and integrating the above expression, the deflection in both sections is obtained in the form of generalised constants, which can be specified by imposing boundary conditions. In particular, referring to Fig. 4(c), the deflection and rotation at the end B are $y_2(x_2 = 0) = 0$ and $y_2'(x_2 = 0) = 2M_2/K_B$, respectively. The deflection and rotation just before and after the step-wise thickness transition section are equal to maintain beam continuity, i.e. $y_2(x_2 = l_E^+) = y_2(x_2 = l_E^-)$ and $y_2'(x_2 = l_E^+) = y_2'(x_2 = l_E^-)$. Lastly, the deflection at the mid-span is set as $y_2(x_2 = l/2) = \delta$. Using these boundary conditions in the generalised deflection equations, the integration constants are determined and back-substituted to get an equation that predicts the critical force P_b triggering elastic buckling in the strut BD

$$\frac{\sqrt{\eta^3}}{\sqrt{P_b E_s I_H}} \tan\left(\lambda_H \frac{l\xi}{2}\right) \tan\left(\lambda_E \frac{l(1-\xi)}{2}\right) + \frac{1}{K_B} \tan\left(\lambda_H \frac{l\xi}{2}\right) - \frac{1}{\sqrt{P_b E_s I_H}} + \frac{1}{K_B} \sqrt{\frac{1}{\eta^3}} \tan\left(\lambda_E \frac{l(1-\xi)}{2}\right) = 0. \tag{17}$$

Eq. (17) can be solved numerically to obtain the critical force P_b, from which the buckling stress of the stepped strut hexagonal honeycomb is calculated as $(\sigma_b)_{SS} = P_b/(\sqrt{3}l)$. It should be noted that Eq. (17) can capture both the local buckling of only the middle section or the global buckling of the entire strut. The buckling stress of the stepped strut hexagonal lattice can be normalised by that of the regular honeycomb, Eq. (3), to assess whether material redistribution enhances the buckling strength. The resulting buckling strength specific ratio, $(\sigma_b)_{SS}/(\sigma_b)_U$, is plotted in Fig. 5. The maximum increase in buckling strength obtained is 3.8% for the geometric parameters $\xi = 0.50$ and $\eta = 0.85$, thus suggesting that material redistribution through variable cross-sections is almost ineffective when the failure mechanism is driven by axial force in the strut. As expected, the specific ratio is one when the struts assume uniform thickness, i.e. $\xi = 0$, $\xi = 1$, and $\eta = 1$.

2.3.1. Critical relative density

During the deformation of honeycombs under uniaxial compression, the struts may undergo elastic buckling or plastic yielding depending upon their aspect ratio. The maximum relative density at which the lattice undergoes buckling is termed critical relative density, $\overline{\rho}_c$. This can be determined by equating the lattice's buckling strength and the plastic strength. For the regular hexagonal lattice, the critical relative density is given as [16]

$$(\overline{\rho}_c)_U = 2\sqrt{3}\,\frac{\sigma_{ys}}{E_s}, \tag{18}$$

which depends on the constituent material properties. Considering the properties of the additively manufactured polymeric material used for the experimental validation of Section 5, $E_s = 893.15$ MPa and $\sigma_{ys} = 39$ MPa, Eq. (18) yields $\overline{\rho}_c = 0.15$.

Similarly, the critical relative density for the hexagonal lattice with stepped struts can be obtained to understand the transition between

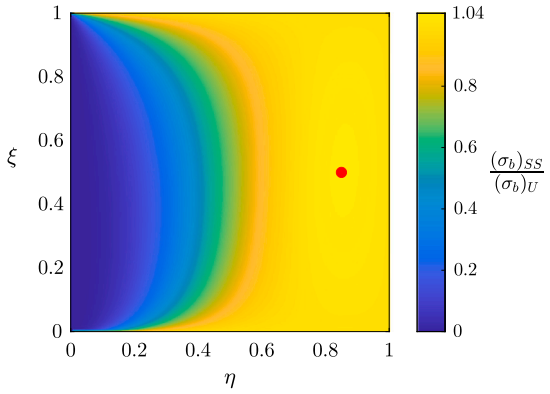

Fig. 5. Contour plot of normalised buckling strength, $(\sigma_b)_{SS}/(\sigma_b)_U$ of stepped strut hexagonal honeycomb as a function the geometric design parameters ξ and η. The parameters combination maximising the strength value is highlighted with a red circle, given by $\xi = 0.50$ and $\eta = 0.85$, for which $(\sigma_b)_{SS}/(\sigma_b)_U = 1.038$.

buckling and plastic failure under uniaxial compressive loading. Since the expression for the buckling behaviour of stepped strut honeycombs is not in a closed form, it is solved numerically for the entire range of the geometric parameters, ξ and η, and is compared with the value of the plastic strength to determine the critical relative density. A comparison of buckling and plastic strengths is performed for relative densities ranging from 0.01 to 0.25, with a resolution of 0.01, to assess the critical failure mode as a function of geometrical parameters ξ and η. Three different failure modes can be observed for the chosen constitutive material properties, as shown in Fig. 6. For relative densities lower than 0.15, the stepped strut hexagonal lattice undergoes only buckling for any value of ξ and η, Fig. 6(a). For $\overline{\rho}_{SS} > 0.15$, the lattice can either buckle, fail by plastic hinge formation at the node, or by plastic hinge formation at the transition section, depending upon the values of ξ and η, as shown in Fig. 6(b)-(d). The critical relative density for the stepped strut hexagonal lattice can be obtained for any particular combination of ξ and η where the failure mode transitions between buckling and plastic failure using the maps in Fig. 6 and those that can be created at other relative densities. Each failure map, created at a specific relative density, highlights the parameter combinations at the transition of regions that depict the critical relative density corresponding to the map's specified relative density. While moving towards higher relative densities, the buckling region in the design space diminishes, leading to more parameter combinations to enable the lattice to fail plastically. A relative density could exist above which buckling failure no longer occurs for any combination of the design parameters, and the struts only collapse plastically. However, this would happen at higher relative densities well beyond the conventional relative density limit for cellular solids (30%) for which Euler Bernoulli's beam theory will not be sufficiently accurate. Within such relative density limit for cellular solids, for the polymeric material considered, a combination of design parameters always exists that enable elastic buckling failure, especially at low η. It should be noted that the exact relative density at which buckling failure no longer occurs depends on the constituent material. For example, in materials like stainless steel, which have higher yield strengths and stiffness, the buckling region diminishes more quickly, and the lattice may experience only plastic collapse at densities lower than 30%, further reducing the likelihood of buckling failure. The maps also differentiate the regions of the design space where plastic failure occurs either by plastic hinge formation at the node or at the transition section, separated by the curve defined through $\xi = \eta^2$. It should be noted that the plots in Fig. 6 only refer to the specific constitutive material used for the experiments and can significantly change if a different material is selected.

3. Multi-objective optimisation

The mechanical properties of honeycomb with redistributed material analysed in the previous section show enhanced stiffness, plastic and buckling strengths. However, each of these properties was maximised independently from the others, and their maximum values occurred at a different combination of parameters ξ and η. Maximising several mechanical properties simultaneously is advantageous for engineering applications. Hence, multi-objective optimisation is employed in the following to identify the set of Pareto optimal configurations and select a unique combination of design parameters that maximises both the stiffness and strength of the hexagonal lattices with material redistribution. The objective functions in the multi-objective optimisation are the normalised stiffness and strength, while the design variables are ξ and η, both of which are defined within the range (0, 1]. These variables control the structural configuration and influence the performance metrics (i.e., stiffness and strength) during optimisation. As no explicit constraints are imposed during the optimisation, the algorithm is free to explore all feasible configurations within the defined bounded range of the design variables. The shape of the Pareto front, the optimal geometric parameters and the corresponding values of mechanical properties depend on the failure mechanism, either buckling or plastic hinge formation, which is inherently linked with the relative density $\overline{\rho}$. Based on the previous results, a MATLAB script has been developed to obtain the plots in Fig. 7, where each point represents one combination of geometrical parameters ξ and η, and normalised stiffness and strength ratios against these points are plotted along the horizontal and vertical axes. Each geometric parameter, ranging from 0 to 1, is computed with a resolution of 0.01, so that 10000 designs are evaluated. In each plot, the Pareto front is represented by the top-right domain's border between the maximum stiffness and maximum strength, highlighted with purple and black circles, respectively. To identify a single configuration that maximises both stiffness and strength from those lying on the Pareto front, a linear scalarisation of the multi-objective optimisation problem is carried out by formulating a single-objective optimisation problem such that Pareto optimal solutions to the multi-objective optimisation problem are optimal solutions for the single-objective optimisation problem. Hence, the script computes the weighted normalised stiffness and normalised strength, $w_1 E_{SS}/E_U + w_2 \sigma_{SS}/\sigma_U$, where $\sigma_{SS} = \min[(\sigma_p)_{SS}, (\sigma_b)_{SS}]$ and $\sigma_U = \min[(\sigma_p)_U, (\sigma_b)_U]$, for each point on the Pareto front, and the point with the maximum value is identified. In this work, we consider equal weight for the two properties, namely $w_1 = w_2 = 1$. Hence, the optimal configuration based on the set criterion is represented by a red circle in the plots of Fig. 7. However, since we provide the Pareto optimal configurations, another choice of the optimal point can also be made, depending upon the criteria and preferences of the designer.

For $\overline{\rho} < 0.15$, the dominant failure mode is elastic buckling for any value of ξ and η, as seen in Fig. 7(a). It can be observed that the plot in Fig. 7(a) is skewed towards high values of stiffness, which shows that the increase in stiffness of the stepped strut hexagonal lattice is significantly more than the maximum increase in buckling strength, for the reasons reported in the previous Section. The maximum increase in stiffness is 37.8% obtained at $\xi = 0.36$ and $\eta = 0.54$, for which the buckling strength is $(\sigma_b)_{SS} = 0.78(\sigma_b)_U$. Whereas, the maximum increase in buckling strength is 3.08%, obtained at $\xi = 0.5$ and $\eta = 0.85$, for which the elastic stiffness results $E_{SS} = 1.17E_U$. Based on the script and set criterion to select an optimal configuration on the Pareto front, for any $\overline{\rho} < 0.15$, the selected point is at $\xi = 0.51$ and $\eta = 0.73$, which gives the maximum possible increase in the stiffness, 29%, while keeping the buckling strength the same as that of the uniform thickness honeycomb, $(\sigma_b)_{SS} = (\sigma_b)_U$.

For the intermediate cases, representative parameter combination plots at the relative densities $\overline{\rho} = 0.17$ and $\overline{\rho} = 0.20$ are shown in Fig. 7(b)-(c). As the strength for these intermediate cases occurs either via elastic buckling or plastic failure, the maximum strength achievable depends on the relative density. It can be observed that the increase in

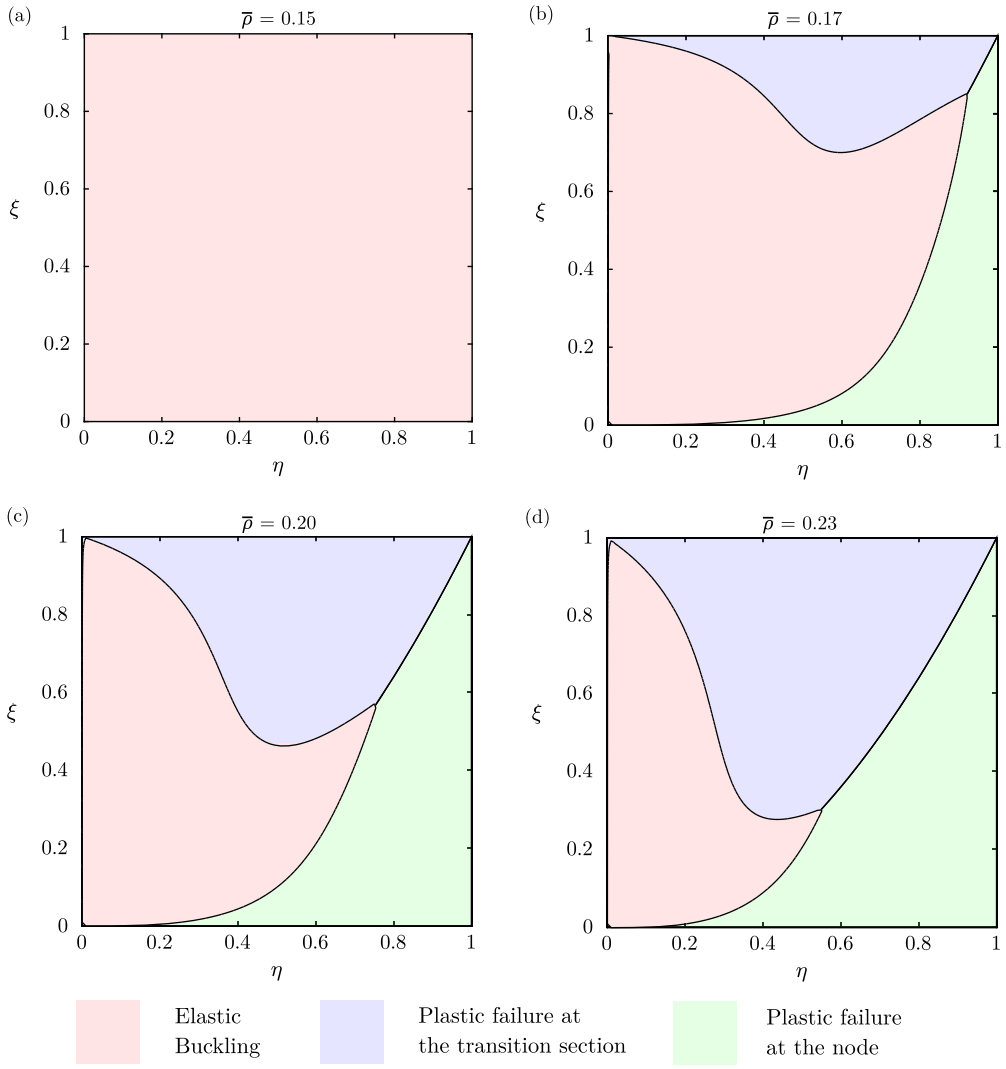

Fig. 6. Failure maps for stepped strut hexagonal lattice at various relative densities: (a) $\overline{\rho} = 0.15$, (b) $\overline{\rho} = 0.17$, (c) $\overline{\rho} = 0.20$, (d) $\overline{\rho} = 0.23$. Different colours highlight failure by (i) elastic buckling (light red area), (ii) plastic hinge formation at the node (light green area) and (iii) plastic hinge formation at the step-wise transition section, $x = l_E$ (light blue area).

stiffness of the stepped strut hexagonal lattice remains the same, irrespective of the relative density. However, the increase in strength varies with the relative density, generally increasing while ascending from the relative density $\overline{\rho} = 0.15$. For the relative densities below 0.15, the maximum strength achievable is the same as the lattice buckles for all combinations of ξ and η. For relative densities above 0.15, until $\overline{\rho} = 0.22$, the shape of the domain representing all possible design combinations and its related Pareto front change. The maximum normalised strength of the stepped strut hexagonal lattice remains between the maximum gain observable with elastic buckling failure mode (3.08%), and the maximum gain associated with plastic hinge formation (37.6%). The maximum increase in strength is achieved at relative densities above 0.22, at which plastic hinge formation becomes the dominant failure mode for any design combination on the Pareto front. Above $\overline{\rho} = 0.22$, the Pareto front does not change. The optimal points at the relative densities 0.17 and 0.20 yield an increase of 30.1% and 30.8% in stiffness, and an increase of 12.2% and 31.0% in strength, at $\xi = 0.58$ and $\eta = 0.83$, and $\xi = 0.56$ and $\eta = 0.75$, respectively.

To exemplify a representative case beyond a relative density of 0.22, a stepped strut hexagonal lattice with a relative density of 0.23 is chosen and plotted in Fig. 7(d), which corresponds with the failure map shown in Fig. 6(d). As obtained in the previous Section, the maximum increase in stiffness is 37.8% obtained at $\xi = 0.36$ and $\eta = 0.54$, for which the plastic strength is $(\sigma_p)_{SS} = 1.17(\sigma_p)_U$. Whereas, the maximum increase in plastic strength is 37.6% obtained at $\xi = 0.45$ and $\eta = 0.67$, for which the elastic stiffness results $E_{SS} = 1.31E_U$. The single point that maximises both stiffness and plastic strength occurs at $\xi = 0.36$ and $\eta = 0.60$, with a 36.3% increase in the stiffness and a 36.5% increase in the plastic strength with respect to regular honeycomb, regarded as optimal configuration. The sensitivity of the objective function is also evaluated at the optimal configuration by analysing the partial derivatives of normalised stiffness and strength with respect to the parameters ξ and η, computed as $\partial_\xi(E_{SS}/E_U) = 0.07, \partial_\xi(\sigma_{SS}/\sigma_U) = 0.34, \partial_\eta(E_{SS}/E_U) = -0.20, \partial_\eta(\sigma_{SS}/\sigma_U) = -0.50$ [4]. The analysis depicts that the variation in the objective function is more responsive to the strut thickness ratio η, as compared to ξ. The local sensitivity analysis also highlights the direct relation of the objective function with ξ and the inverse relation with η.

4. Numerical modelling

Finite element (FE) analyses were carried out to validate the analytical predictions obtained in the previous sections. Two complementary FE simulation sets were run to obtain (i) the periodic response through unit cell analysis as a direct comparison of the previous analytical results and (ii) the behaviour on finite lattices, which enables the quantifica-

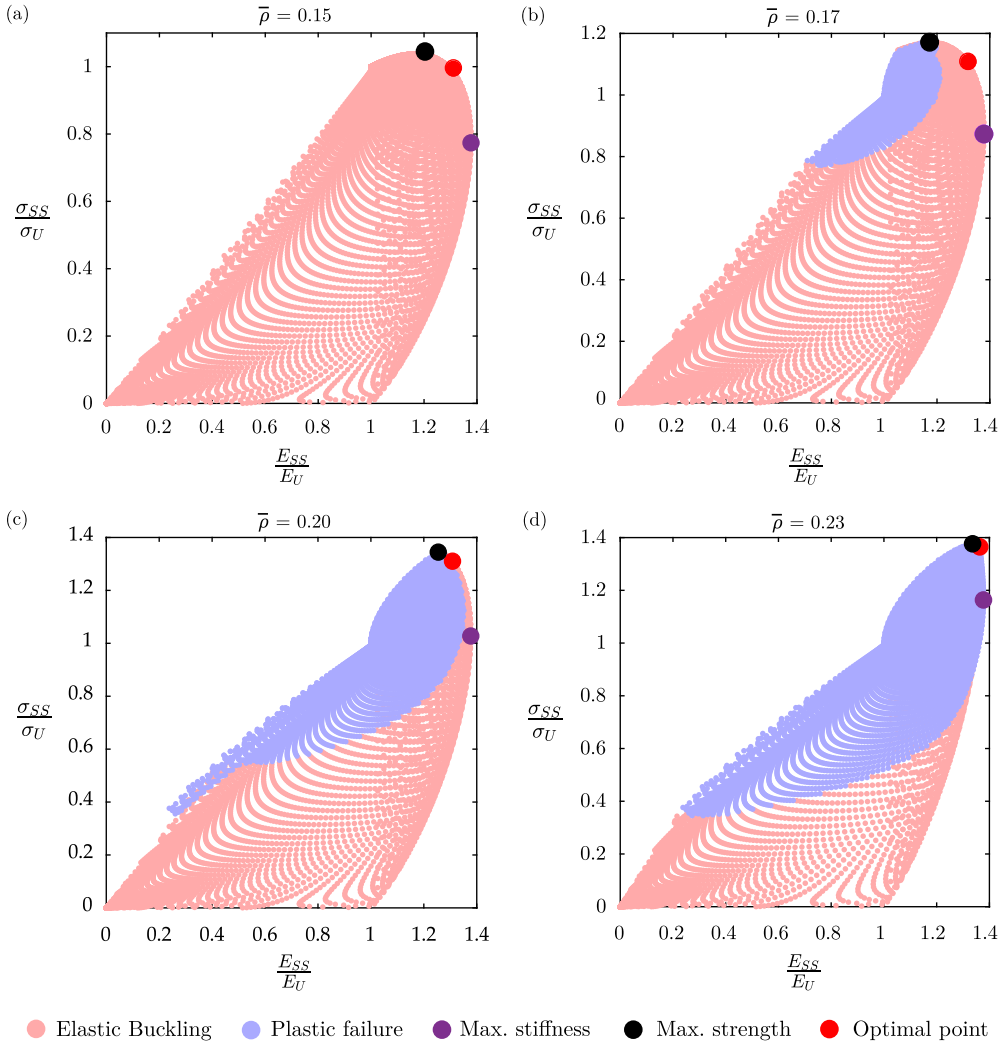

Fig. 7. Optimisation of normalised stiffness and strength of honeycomb with stepped struts at relative densities (a) $\overline{\rho} = 0.15$, (b) $\overline{\rho} = 0.17$, (c) $\overline{\rho} = 0.20$, (d) $\overline{\rho} = 0.23$. Each combination of material parameters ξ and η is represented by one dot, whose colour represents either plastic failure (light blue) or elastic buckling (light red). The points of maximum stiffness, maximum strength and optimal configuration are shown through purple, black and red circles, respectively.

tion of the edge effects and will be directly compared with experiments, Section 5.

Two-dimensional parametric models of the (i) unit cells and (ii) finite lattices were created using SolidWorks (Dassault Systèmes), with parameterisation based on input design parameters (η, ξ) and corresponding t/t_H values for a fixed length l, generating a range of hexagonal honeycomb configurations. The generated geometry was then imported from a `.step` file into Abaqus 2018 (Dassault Systèmes), where a 2D planar deformable part was established. Material properties in the finite element models were set to match the properties of the material employed in the experiments, modelled as an elastic perfectly plastic material with Young's modulus $E_s = 893.15$ MPa, yield strength $\sigma_{y,s} = 39$ MPa, and Poisson's ratio $\nu_s = 0.3$, as determined by the material characterisation, Section 5. Notably, the performance metrics used in this study, namely the stiffness and strength of variable-thickness honeycombs normalised with respect to the uniform lattice, are independent of the material constants. The entire lattice structure was assigned a homogeneous solid section with a unit thickness, and the part was discretised using linear plane stress elements (`CPS3` and `CPS4R`). A systematic mesh convergence study was conducted using the quantities of interest, stiffness and strength, to ensure the accuracy and reliability of our numerical results, following a threshold criterion of less than 2%. The element size was set to $0.1\,t_{min}$, with t_{min} representing the minimum strut thickness. This approach ensured a minimum of ten elements across the strut's smallest thickness, balancing mesh convergence and computational efficiency. To prevent excessive node refinement, a minimum size control was set at 10% of the global element size. To maintain mesh quality and reduce element distortion, especially during the elastic and plastic softening phases, the Arbitrary Lagrangian-Eulerian (ALE) adaptive meshing tool was employed. The analyses comprised two steps: first, a `Linear Perturbation` step to predict the buckling strength and mode, followed by a `General Static` step to determine the quasi-static engineering stress-strain response. These steps allowed for calculating the lattice's effective elastic stiffness, buckling and plastic strengths. Post-processing procedures extracted the reaction force in the loading $\tilde{y}$-direction and the displacements in the horizontal $\tilde{x}$- and vertical $\tilde{y}$-directions, from which engineering effective stresses and strains were computed.

Boundary conditions were configured to replicate the uniaxial compression test, up to an effective uniaxial compressive strain $\epsilon_{22} = -20\%$ was reached in the vertical $\tilde{y}$-direction. The boundary conditions differed depending on the unit cell or finite lattice simulation. FE analyses on a representative unit cell allowed to minimise computational cost while determining the bulk mechanical characteristics of the infinite hexagonal lattice. The unit cell shape was selected to possess translational symmetries and specifically avoid any reflective symmetries to simplify boundary conditions and prevent the need for distinct boundary formulations for different loading conditions, as documented by Li et al. [36]. Also, an appropriate unit cell should not induce an in-plane

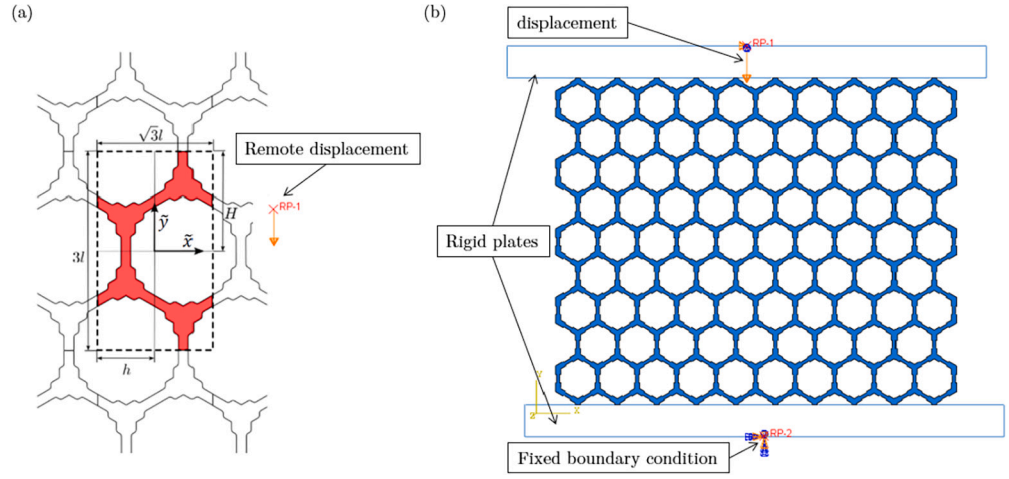

Fig. 8. (a) Rectangular unit cell used in the finite element analysis of hexagonal honeycomb, (b) FE model for finite lattice.

anisotropy, as the hexagonal lattice is known to have isotropic in-plane properties in the elastic regime [37,38]. In adherence to these criteria, a rectangular unit cell with translational symmetries in both the horizontal ($\tilde{x}$) and vertical ($\tilde{y}$) directions was selected. A set of equation constraints on displacement and rotations was set to impose periodic boundary conditions, effectively replicating the behaviour of an infinite lattice, as in Fig. 8(a). Therefore, two equations relate the relative translational degrees of freedom, given by u_1 and u_2, of each side-pair to remote uniaxial strains ε_{22} in the $\tilde{y}$ directions

$$u_1|_{\tilde{x}=-h} - u_1|_{\tilde{x}=h} = 0\,, \qquad u_2|_{\tilde{x}=-h} - u_2|_{\tilde{x}=h} = 0, \tag{19}$$

$$u_1|_{\tilde{y}=-H} - u_1|_{\tilde{y}=H} = 0\,, \qquad u_2|_{\tilde{y}=-H} - u_2|_{\tilde{y}=H} = -2H\varepsilon_{22}, \tag{20}$$

where $h = \sqrt{3}l/2$ and $H = 3l/2$ are the characteristic sizes of the unit cell along the horizontal and vertical directions, respectively. Since the boundary nodes of each side-pair are coupled, an additional set of equations must be imposed on their rotational degree of freedom ω_{12}

$$\omega_{12}|_{\tilde{x}=-h} - \omega_{12}|_{\tilde{x}=h} = 0\,, \qquad \omega_{12}|_{\tilde{y}=-H} - \omega_{12}|_{\tilde{y}=H} = 0. \tag{21}$$

Additional details about the equation constraints can be found in the work by Kuszczak et al. [39], while other information regarding material properties are reported below.

FE simulations on finite lattices were carried out to complement the experimental validation, accounting for the finite size of the manufactured honeycombs (10x9 cells) and the influence of edge effects on their mechanical properties, as shown in Fig. 8(b). To mimic the experimental setup on finite lattices, constrained vertical displacement at the bottom surface and prescribed vertical displacement at the top surface were imposed. To achieve this, rigid plates were introduced at the top and bottom of the lattice, with hard contact conditions and a friction coefficient ($\mu = 0.3$) between the rigid body and the lattice surfaces. Self-contact property was activated on all lattice surfaces to detect any contact between struts beyond elastic or plastic failure. Although it was outside the scope of this work, it is worth noting that simulations conducted on finite lattices enabled the accurate characterisation of post-failure behaviour in honeycombs, predicting the layer-by-layer failure and densification, aspects not captured through unit cell analysis. The results of the FE analyses on unit cells and finite lattices are reported alongside the experimental measurements in Section 6.

5. Experiments

Experimental compression tests were carried out on optimised configurations to validate the theoretical results. Finite lattices of regular and stepped strut hexagonal honeycombs were manufactured at two relative densities of $\overline{\rho} = 0.10$ and $\overline{\rho} = 0.23$, representative of elastic buckling and plastic failure, respectively. They were tested to determine and compare their mechanical properties with analytical and numerical predictions.

Table 1
Properties of Durable V2 material cured for 10 hours [39].

E_s (MPa)	$\sigma_{y,s}$ (MPa)
893.15 ± 99.2	39 ± 3.22

5.1. Fabrication

Hexagonal honeycomb lattices were manufactured using a Form 3 3D printer from Formlabs, employing the Low Force Stereolithography (LFS) additive manufacturing process. This method utilises photopolymer resins and a laser projection to build solid structures layer by layer. In this work, Durable V2 resin was chosen for producing specimens due to its stress-strain behaviour approximating an engineering elastic perfectly-plastic response [40], which aligns with the material model assumed in the preceding sections. The mechanical properties of this material have been previously investigated and reported in [39], with a summary of the average properties provided in Table 1.

The lattice specimens were constructed as finite lattices comprising 10x9 cells (width x height) to ensure their properties were representative of those in an infinite lattice with 90% accuracy, as referenced in [41]. To prevent out-of-plane buckling, the depth of all lattice structures was maintained at 20 mm. At a relative density of 0.23, the minimum strut thickness (t for uniform and t_H for non-uniform cell) was held constant at 0.75 mm, with strut lengths of 5.11 mm, and 5.95 mm, for regular and stepped strut honeycombs, respectively. Additionally, the horizontal sizes of a representative rectangular cell (measured as $\sqrt{3}l$, with l the strut length) were set at 9.8 mm and 10.5 mm for regular and stepped strut lattices, respectively. The resulting dimensions of the lattice structures were 96.83x78.39 mm for the regular honeycomb and 96.83x78.39 mm for the stepped strut lattice. Likewise, at a relative density of 0.10, the minimum strut thickness was maintained at 0.5 mm, with strut lengths of 5.5 mm and 6.2 mm, so that the cell sizes were 10 mm and 12.6 mm for regular and stepped strut lattices, respectively. The resulting dimensions of the lattices were 100.5x81.3 mm for the regular honeycomb and 100.5x123.6 mm for the stepped strut design. It is worth noting that the length of the strut and the cell size were adjusted to maintain consistent minimum thickness across all relative density levels, prioritising ease of manufacturability. After the 3D printing process, all specimens underwent a 15-minute wash in 99.9% isopropyl alcohol

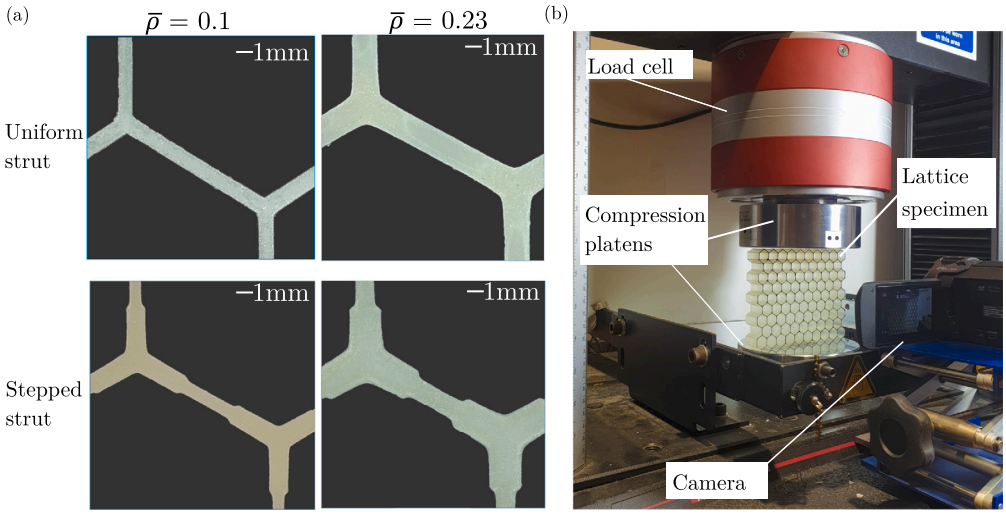

Fig. 9. (a) Microscopic images of the 3D printed hexagonal lattices with uniform and stepped struts at relative densities of $\overline{\rho} = 0.1$ and $\overline{\rho} = 0.23$. (b) Experimental setup for the compression testing of the finite hexagonal honeycombs.

Table 2
Comparison of stiffness and strength between regular and stepped strut hexagonal honeycombs, obtained through analytical predictions, numerical analysis of unit cells and finite lattices, and experimental measurements. Improvement refers to the gain obtained in the stepped strut honeycomb (second to last column) if compared with the uniform (third to last column) lattice of similar relative density.

		Uniform (MPa)	Stepped strut (MPa)	Improvement (%)
		$\overline{\rho} = 0.105$	$\overline{\rho} = 0.109$	
Stiffness, E	Analytical	1.55	2.2	41.9
	FEA unit cell	1.32	1.87	41.7
	FEA finite lattice	1.24	1.71	37.9
	Experiment	1.19±0.019	1.62±0.13	35.8
Strength, σ_b	Analytical	0.135	0.149	10.3
	FEA unit cell	0.131	0.137	4.5
	FEA finite lattice	0.126	0.1343	6.3
	Experiment	0.12±0.0013	0.126±0.003	5
		$\overline{\rho} = 0.235$	$\overline{\rho} = 0.229$	
Stiffness, E	Analytical	17.44	22.29	27.8
	FEA unit cell	15.45	19.1	23.6
	FEA finite lattice	15.03	18.48	22.9
	Experiment	14.44±0.43	17.65±0.21	22.2
Strength, σ_p	Analytical	1.08	1.41	30.8
	FEA unit cell	1.05	1.29	23.2
	FEA finite lattice	0.99	1.22	22.7
	Experiment	0.95±0.006	1.15±0.029	21.2

(IPA) to remove excess liquid resin from their surfaces. Subsequently, they were cured for 10 hours under ultraviolet (UV) light in a heated chamber at 80 °C. This curing step was crucial for the material to attain its maximum mechanical performance and stabilise its properties. Shorter curing times were found to be insufficient in guaranteeing reliable stress-strain responses. In total, three samples of both uniform and non-uniform lattices were printed for relative densities of 0.10 and 0.23, resulting in a total of twelve finite honeycomb specimens. All lattices were printed with the same orientation, minimising the influence of the printing direction on the mechanical properties.

5.2. Compression tests

Before commencing compression tests, a thorough examination of the 3D-printed lattice specimens was conducted. Using a digital microscope, each specimen was inspected for any discernible defects or cracks that could potentially influence the outcomes of the tests, as depicted in Fig. 9(a). From the figure, it is possible to observe the good quality of the manufactured specimens, which closely matched the input design. The exception is represented by the stepped strut honeycombs, where it was difficult to obtain a sharp step-wise transition between the two thicknesses; nevertheless, such imperfection had a negligible influence on the results, see also Section 6. In addition, some representative samples underwent X-ray computed tomography (XCT) scanning to ensure the absence of internal porosity within the lattice struts. Several key measurements were taken on each specimen, including their initial depth, width, and height. These measurements served as parameters required for the subsequent calculation of the engineering stress and strain during the compression tests. The densities of the lattices were determined by weighing the specimens and dividing their mass by the effective volume of the lattices. The ratio of the lattice density to that of the constituent material ($\rho_s = 1.078$ g/mm^3) was computed to establish the experimental relative densities of the lattices. The resultant values for the experimental relative densities of both the uniform thickness and non-uniform lattices are presented in Table 2.

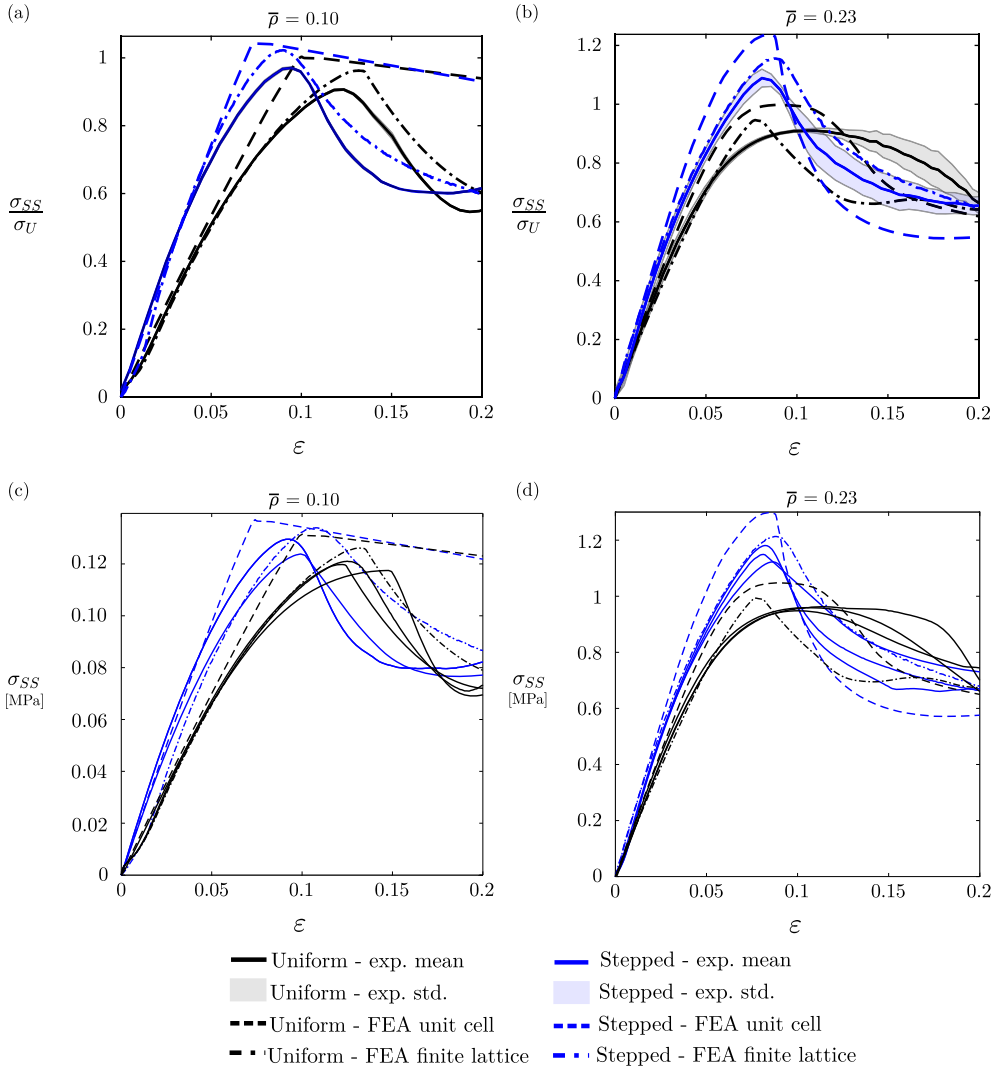

Fig. 10. Compressive stress-strain response of hexagonal honeycombs with uniform (black) and stepped strut (blue) thickness profile for $\overline{\rho} = 0.10$ (left) and $\overline{\rho} = 0.23$ (right). Experimental measurements (average and standard deviation, solid curves) are reported together with FE results for unit cell (dashed curves) and finite lattice (dot-dashed curves) in normalised stress (a-b) and engineering stress (c-d) vs strain plots.

The lattice specimens were subjected to quasi-static uniaxial compression testing using an Instron 5985 electromechanical testing machine. A uniform strain rate was set to maintain consistency with the conditions of the uniaxial tests performed for material characterisation [39], with a crosshead speed of 5.5 mm/min. Each lattice was positioned between the compression platens, ensuring that the applied load acted vertically on the top surface of the lattice. Before the actual testing, a pre-load of 5 N was applied to eliminate any initial slack in the specimen. The effective engineering strain within the lattice was calculated by dividing the vertical displacement of the machine crossbeam by the lattice's initial height. The engineering stress was computed by dividing the force measured by the load cell by the effective cross-sectional area of the lattice, denoted as LxD, where L is the width of the specimen. Data on displacement and force were recorded at a frequency of 1 Hz. Compression was continued until an effective engineering strain value of 20% was reached in the lattices. The deformation behaviour during compression tests was visually captured using a high-definition single-lens optical camera. The effective elastic modulus was derived from the slope of a linear regression model applied to the linear portion of the stress-strain curve. The strength of the lattice, which could manifest as either buckling or plastic collapse depending on the relative density, was determined by identifying the first peak stress on the stress-strain curve. A total of three tests were conducted for each type of honeycomb, and the average and standard deviation of stiffness and strength were calculated.

6. Results and discussion

The results of the compression tests on lattices with a relative density of 0.10 and 0.23, featuring uniform thickness and struts with redistributed material, are depicted in Fig. 10 as engineering effective stress vs. strain plots. Alongside these experimental results, predictions generated by finite element analyses, based on unit cell and finite specimen models, are also presented. The stress values have been normalised by the strength of the uniform hexagonal unit cell obtained from FEA, denoted as $(\sigma_b)_U$ and $(\sigma_p)_U$ for buckling and plastic failure, respectively. This normalisation serves to highlight the advantages acquired through the redistribution of strut material.

The responses of finite lattices undergoing buckling, with a representative relative density of $\overline{\rho} = 0.10$, lower than the critical relative density, are reported in Fig. 10(a), showing the average stress-strain responses, alongside the standard deviation, for both uniform and material-redistributed honeycomb. These specimens exhibit an initial linear region, from which the effective stiffness is calculated, followed by the attainment of a maximum peak stress and, subsequently, a softening phase. In this context, the peak stress corresponds to the buckling

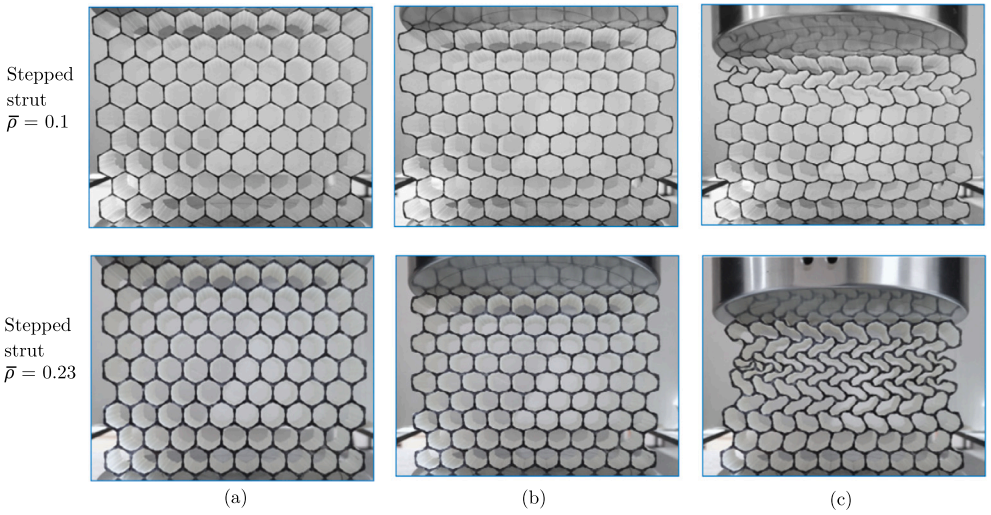

Fig. 11. Compressive deformation behaviour of hexagonal honeycombs with stepped strut thickness profile for $\overline{\rho} = 0.10$ and $\overline{\rho} = 0.23$, taken at (a) $\varepsilon = 0.0$, (b) peak stress, and (c) $\varepsilon = 0.2$.

stress, as substantiated by numerical predictions and specific experiments wherein the samples were unloaded right after reaching the peak stress, reverting to their initial configuration without displaying any residual plastic deformation. Once the buckling strength is achieved, there occurs an initial post-buckling elastic response, and if the experiment is continued to higher strains, an elasto-plastic phase follows.

The average mechanical properties of the uniform lattice have been derived from stress-strain data obtained in three tests, yielding a compressive modulus of $E_{U,0.10} = 1.19 \pm 0.019$ MPa and a buckling strength of $(\sigma_b)_{U,0.10} = 0.12 \pm 0.0013$ MPa. These properties serve as reference benchmarks for evaluating the mechanical characteristics of honeycombs with optimised shapes. For the stepped strut honeycomb, the results are as follows: $E_{SS,0.10} = 1.62 \pm 0.13$ MPa and $(\sigma_b)_{SS,0.10} = 0.126 \pm 0.003$ MPa. The improvement in stiffness compared to the measured properties of the uniform honeycomb is 35.8% for the stepped strut honeycomb. Additionally, there is a 5% increase in buckling strength for the stepped strut honeycomb. The experimental measurements for the lattices closely align with the corresponding FE predictions, especially those for the finite lattice.

The comparison between the experimental and numerical behaviour of lattices undergoing plastic failure is reported in Fig. 10(b), which shows the effective engineering stress-strain curves of honeycomb with a representative relative density of $\overline{\rho} = 0.23$. The elastic modulus of the lattice has been computed by analysing the linear elastic region, which is succeeded by a nonlinear region preceding the peak stress point. In this pre-peak stress region, the lattice yields at the nodes due to stress concentration. Upon reaching the maximum load and stress levels, complete yielding of the material across at least one strut cross-section occurs, forming a plastic hinge and inducing plastic collapse. Beyond this critical point, a softening phenomenon commences, causing a decline in stress. Simultaneously, deformation becomes unsymmetrical and localised. When examining the finite uniform honeycomb's experimental and finite element (FE) results, the initial softening behaviour corresponds to the collapse of a single row of cells, which would be followed, if the simulations and experiments are carried out until higher strains, by subsequent hardening phenomenon caused by strut contact, until another row of cells fails, characterised by a subsequent and smaller decrease in stress. This deformation mechanism would persist until all rows have sequentially collapsed and come into contact with one another, resulting in densification and a significant increase in stress. However, this is not depicted in the graphical representation. A total of three tests were executed on specimens with uniform strut thickness, and the average values for the calculated elastic modulus and plastic strength were determined to be $E_{U,0.23} = 14.44 \pm 0.43$ MPa and $(\sigma_p)_{U,0.23} = 0.95 \pm 0.006$ MPa, respectively. As before, these compression properties serve as a benchmark for the evaluation of the honeycomb with solid material redistribution. The honeycombs featuring optimised strut profile exhibit elevated stiffness and stress values, thereby substantiating the efficacy of the optimisation procedure. Moreover, these honeycombs display a qualitatively similar response to that of the uniform honeycomb up to the point of peak stress. However, after the plastic collapse induced by the formation of plastic hinges, a distinctive softening phase emerges, characterised by a plateau stress that precedes the densification phase. This particular response, which was outside the scope of this study and could represent another property to optimise for, arises from the concurrent failure of multiple rows, in contrast to the row-by-row collapse observed in the uniform honeycomb.

Such simultaneous collapse of multiple rows can be attributed to the redistribution of material within the lattice struts. Due to the optimised strut shape, which allocates more material towards the nodes and reduces material in the strut's central portion, the lattice nodes exhibit higher resistance and require greater stress to deform. In contrast, the strut's thinner middle section necessitates less stress to deform. Consequently, the middle portion of the cell struts in all rows initiates deformation before the stress required for node deformation is achieved. Once the plastic collapse stress is reached, this leads to an almost simultaneous collapse of the lattice rows. Notably, sporadic and abrupt variations in the plateau region of the stress-strain response are discernible, attributable to the fracturing of certain struts. The average elastic modulus and plastic strength for the honeycomb with stepped strut, with a relative density of $\overline{\rho} = 0.23$, were determined from three tests, resulting in $E_{SS,0.23} = 17.65 \pm 0.21$ MPa and $(\sigma_p)_{SS,0.23} = 1.15 \pm 0.029$ MPa, respectively. The improvements in stiffness and plastic strength compared to the measured properties of the uniform honeycomb amount to 22.2% and 21.2%, respectively, in excellent accordance with numerical predictions.

From Fig. 10, it is evident that the FE results of the finite-sized lattices provide a more accurate representation of the experimental response. This improved accuracy can be attributed to the FEA's consideration of the reduced stiffness and strength resulting from edge effects and the post-failure behaviour with finite rows. In contrast, the unit cell analysis results in a slightly stiffer and stronger response and fails to predict the row-by-row collapse of the finite specimens with uniform thickness. For both relative densities, the deformed configurations of uniform and stepped strut honeycombs are shown in Fig. 11 for representative strain values.

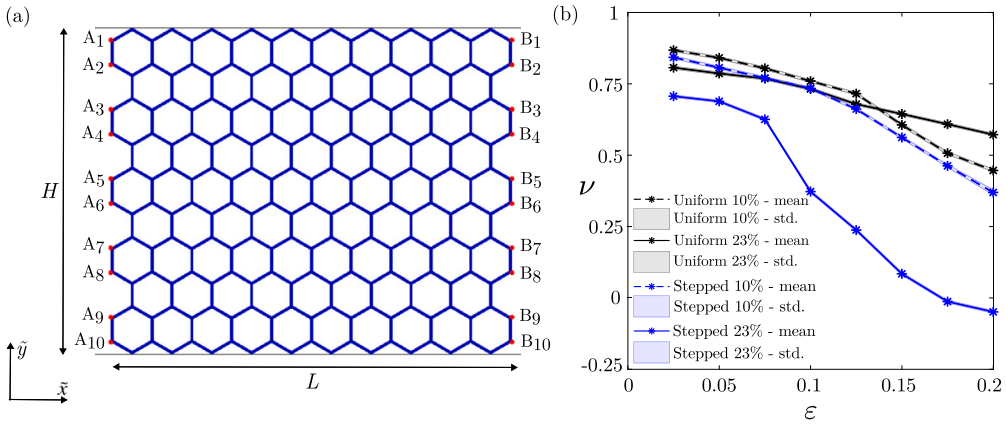

Fig. 12. (a) Schematic of a representative finite lattice with points used to determine the transverse strain, to calculate the Poisson's ratio using Eq. (22), (b) Measured effective Poisson's ratio for hexagonal honeycombs with uniform (black), and stepped strut (blue) thickness profiles for $\overline{\rho} = 0.10$ (dashed) and $\overline{\rho} = 0.23$ (solid).

A summary of the mechanical properties of honeycombs with uniform thickness and optimised stepped-strut shapes is presented in Table 2. This table also compares the experimental properties and those obtained through finite element analyses on unit cells and finite lattices, as well as analytical predictions, all at the same relative densities. Generally, the analytical and numerical properties of honeycombs tend to be higher than the experimental results, with differences of up to 12%. This discrepancy can be attributed to imperfections in manufacturing the tested lattices, which tend to reduce the mechanical response. Furthermore, the theoretical and numerical analyses conducted on unit cells with periodic boundary conditions effectively represent an infinite lattice. In contrast, the experimental properties are acquired through the compression of finite lattices, in which edge effects decrease the mechanical properties. Additionally, the analytical expressions were derived based on the Euler-Bernoulli beam theory, which neglects the effects of shear and axial deformation. This further contributes to the discrepancy between analytical and experimental results. It is worth noting that the experimental results exhibit a very good agreement with the numerical results, given that the finite lattice was designed to represent approximately 90% of the bulk properties.

A notable improvement becomes apparent when comparing the stress-strain responses of the optimised honeycombs with the uniform-thickness honeycomb. For the honeycombs at a relative density of $\overline{\rho} = 0.10$, an increase in stiffness and strength is observed. However, the rise in buckling strength is mainly due to the slightly higher relative density of the non-uniform lattices in the experimental specimens; this explains the higher percentage increase in analytical stiffness and strength compared to the earlier reported improvements. As introduced before, this limitation in the increase of buckling strength is primarily because compressive buckling is mainly dependent on the axial force within the struts. The behaviour also relies on various factors, including changes in the distribution of the second moment of area, the end constraint conditions, and the effective length of the buckling strut. Shifting material towards the nodes leads to an increase in the moment and rotational stiffness of the joint while simultaneously reducing the effective length of the buckling strut and creating weak regions with limited cross-section. The reduction in effective length would theoretically require a higher stress to buckle the strut. However, the rate at which the thickness of the middle section decreases is faster than the decrease in the effective length, which ultimately offsets the overall impact of material redistribution, hindering the enhancement of buckling strength.

The honeycombs with a relative density of $\overline{\rho} = 0.23$, featuring architectures derived from the material redistribution of the stepped strut, exhibit enhanced stiffness and strength compared to the uniform-thickness honeycomb. This increase in mechanical properties can be elucidated by considering the deformation mechanism within the hexagonal lattice. In a hexagonal lattice, the cell walls undergo bending, with the highest bending moment experienced at the nodes. When material from the middle of the strut is shifted towards the node, the second moment of area at the nodal section increases, thus increasing both the stiffness and the plastic strength of the lattice. A similar phenomenon of increased stiffness or plastic strength resulting from the redistribution of strut material has been documented in the literature [28,42,32,43,34]. It is important to acknowledge that when comparing uniform and non-uniform tested lattices, the increase in stiffness and strength could have been even more if the same experimental relative density had been achieved. The slightly higher relative density observed in the regular lattices tends to reduce the overall improvements obtained moderately.

From the experimental compressive deformation response of Fig. 11, it becomes evident that both uniform and non-uniform honeycombs exhibit a significantly high effective Poisson's ratio during the linear elastic phase, which subsequently diminishes and becomes highly strain-dependent after the initiation of the first softening branch, as shown in Fig. 12. The calculation of this ratio involved averaging the measured strain in the transverse direction over the vertical (imposed strain) direction for all the cell rows in the sample, as depicted in Fig. 12. The transverse strain was determined by measuring the pixels in the deformed state in the horizontal direction from the images captured during the experiment and dividing this by the number of pixels in the undeformed state. The formula utilised to compute the Poisson's ratio is

$$\nu = -\frac{\varepsilon_x}{\varepsilon_y} = -\frac{H}{L}\left(\frac{\sum_{i=1}^{10}\left(|\Delta A_{i,x}| + |\Delta B_{i,x}|\right)}{2 \cdot \Delta_y}\right), \tag{22}$$

where the quantities H, L are shown in Fig. 12, while Δ_y is the applied remote displacement on lattice along $\tilde{y}$-axis, whereas $\Delta A_{i,x}$ and $\Delta B_{i,x}$ are the displacements of the selected nodes in lattice along the $\tilde{x}$-axis, as in Fig. 12.

In the case of uniform lattices, the Poisson's ratio ν_U falls within the range of [0.8-0.87] during the linear elastic regime, aligning with the analytical prediction of $\nu_U = 1.0$ [44]. It subsequently decreases and reaches a minimum value of approximately $\nu_{U,\min,0.10} \approx 0.45$ and $\nu_{U,\min,0.23} \approx 0.57$ at the highest imposed strain. Conversely, non-uniform lattices exhibit a lower Poisson's ratio than the uniform lattices at any specific strain. In the linear elastic regime, ν remains positive and constant before consistently reducing to lower values at higher strains, eventually shifting to negative values for $\overline{\rho} = 0.23$. The lowest recorded values are approximately $\nu_{SS,\min,0.10} \approx 0.36$ and $\nu_{SS,\min,0.23} \approx -0.05$ for the stepped strut honeycomb at relative densities of $\overline{\rho} = 0.10$ and $\overline{\rho} = 0.23$, respectively. This auxetic behaviour, which could be part of future optimisation studies, is contingent on the redistribution of material toward the nodes, which results in less deformation in the nodal region compared to the centre of the strut and greater rotation after reaching the peak stress, yielding a difference in stiffness along the strut [45], thereby creating the re-entrant effect.

7. Conclusion

In this work, a 2D hexagonal honeycomb with a modified strut shape with two different thicknesses is studied to understand and quantify the effect of material redistribution on the lattice's stiffness, buckling and plastic strengths. Such stepped strut hexagonal lattices are analysed using an analytical approach based on beam theory to develop formulations that can predict the variation in mechanical properties by material redistribution. The material redistribution is defined using two geometric parameters, ξ and η, and the main mechanical properties are determined as a function of these parameters as well as relative density to obtain Pareto optimal configurations that simultaneously maximise both stiffness and strength with respect to the regular honeycombs. The response of uniform and modified hexagonal lattices is also assessed using numerical and experimental tools, and the results are compared with analytical prediction to validate the analytical formulations. It is demonstrated that a material redistribution can significantly improve the studied properties, especially stiffness and plastic strength, and induce unexpected features in the lattice, such as auxeticity. The choice of the stepped strut profile favoured the analytical treatment, but it is acknowledged it is suboptimal if those properties need to be maximised. Other thickness distributions, such as tapered or with more complex shapes, could be studied to achieve even higher gains than those reported in this study. Although the optimisation is performed on the hexagonal honeycomb only, the approach has the potential to act as a generalised framework for the optimisation of the lattices and can be extended to other unit cell geometries and strut profiles. It provides control and perspective to a designer in terms of the geometrical parameters, which can be tailored to any application.

CRediT authorship contribution statement

F.I. Azam: Writing – review & editing, Writing – original draft, Methodology, Investigation, Formal analysis, Data curation. **P.J. Tan:** Writing – review & editing, Supervision, Project administration, Conceptualization. **F. Bosi:** Writing – review & editing, Supervision, Resources, Project administration, Funding acquisition, Conceptualization.

Declaration of competing interest

The authors declare that they have no known competing financial interests or personal relationships that could have appeared to influence the work reported in this paper.

Acknowledgement

The authors acknowledge support from the EU H2020-MSCA-ITN-2020-LIGHTEN-956547.

Data availability

Data will be made available on request.

References

[1] J.U. Surjadi, L. Gao, H. Du, X. Li, X. Xiong, N.X. Fang, Y. Lu, Mechanical metamaterials and their engineering applications, Adv. Eng. Mater. 21 (3) (2019) 1800864, https://doi.org/10.1002/adem.201800864.
[2] J. Bauer, L.R. Meza, T.A. Schaedler, R. Schwaiger, X. Zheng, L. Valdevit, Nanolattices: an emerging class of mechanical metamaterials, Adv. Mater. 29 (40) (2017) 1701850, https://doi.org/10.1002/adma.201701850.
[3] M. Gei, Z. Chen, F. Bosi, L. Morini, Phononic canonical quasicrystalline waveguides, Appl. Phys. Lett. 116 (24) (2020) 241903, https://doi.org/10.1063/5.0013528.
[4] A. Farrokhabadi, D. Chronopoulos, Composite curved hourglass cellular structures: design optimization for stiffness response and crashworthiness performance, Compos. Struct. 330 (2024) 117834, https://doi.org/10.1016/j.compstruct.2023.117834.
[5] S. Chen, X. Liu, J. Hu, B. Wang, M. Li, L. Wang, Y. Zou, L. Wu, Elastic architected mechanical metamaterials with negative stiffness effect for high energy dissipation and low frequency vibration suppression, Composites, Part B, Eng. 267 (2023) 111053, https://doi.org/10.1016/j.compositesb.2023.111053.
[6] N. Mehreganian, A.S. Fallah, P. Sareh, Structural mechanics of negative stiffness honeycomb metamaterials, J. Appl. Mech. 88 (2021), https://doi.org/10.1115/1.4049954.
[7] Z. Yan, J. Zhu, E. Borisov, A. Riemslag, S.P. Scott, M. Hermans, J. Jovanova, V. Popovich, Superelastic response and damping behavior of additively manufactured nitinol architectured materials, Addit. Manuf. 68 (2023) 103505, https://doi.org/10.1016/j.addma.2023.103505.
[8] J.H. Mueller, J.A. Lewis, K. Bertoldi, Architected multimaterial lattices with thermally programmable mechanical response, Adv. Funct. Mater. 32 (2021), https://doi.org/10.1002/adfm.202105128.
[9] F. Sommese, L. Badarnah, G. Ausiello, A critical review of biomimetic building envelopes: towards a bio-adaptive model from nature to architecture, Renew. Sustain. Energy Rev. 169 (2022) 112850, https://doi.org/10.1016/j.rser.2022.112850.
[10] L. Musenich, F. Libonati, Hierarchical bioinspired architected materials and structures, Extrem. Mech. Lett. 58 (2023) 101945, https://doi.org/10.1016/j.eml.2022.101945.
[11] Y. Wang, H. Qin, Z. Li, J. Dai, H. Cong, S. Yu, Highly compressible and environmentally adaptive conductors with high-tortuosity interconnected cellular architecture, Nat. Synth. 1 (2022) 975–986, https://doi.org/10.1038/s44160-022-00167-5.
[12] X. Xia, C.M. Spadaccini, J.R. Greer, Responsive materials architected in space and time, Nat. Rev. Mater. 7 (2022) 683–701, https://doi.org/10.1038/s41578-022-00450-z.
[13] M.N. Andersen, F. Wang, O. Sigmund, On the competition for ultimately stiff and strong architected materials, Mater. Des. 198 (2021) 109356, https://doi.org/10.1016/j.matdes.2020.109356.
[14] A. Kudo, F. Bosi, Nanographitic coating enables hydrophobicity in lightweight and strong microarchitected carbon, Commun. Mater. 1 (2020), https://doi.org/10.1038/s43246-020-00073-3.
[15] N.A. Fleck, V.S. Deshpande, M.F. Ashby, Micro-architectured materials: past, present and future, Proc. R. Soc. A, Math. Phys. Eng. Sci. 466 (2121) (2010) 2495–2516, https://doi.org/10.1098/rspa.2010.0215.
[16] L. Gibson, M. Ashby, Cellular Solids: Structure and Properties, Cambridge Solid State Science Series, Cambridge University Press, 1999.
[17] L.J. Gibson, M.F. Ashby, G.S. Schajer, C.I. Robertson, The mechanics of two-dimensional cellular materials, Proc. R. Soc. Lond. Ser. A, Math. Phys. Sci. 382 (1782) (1982) 25–42, https://doi.org/10.1098/rspa.1982.0087.
[18] L. Gibson, M. Ashby, J. Zhang, T. Triantafillou, Failure surfaces for cellular materials under multiaxial loads—I. Modelling, Int. J. Mech. Sci. 31 (9) (1989) 635–663, https://doi.org/10.1016/S0020-7403(89)80001-3.
[19] A. Kalamkarov, G. Saha, A. Georgiades, General micromechanical modeling of smart composite shells with application to smart honeycomb sandwich structures, Compos. Struct. 79 (1) (2007) 18–33, https://doi.org/10.1016/j.compstruct.2005.11.026.
[20] R.S. Kumar, D.L. McDowell, Generalized continuum modeling of 2-d periodic cellular solids, Int. J. Solids Struct. 41 (26) (2004) 7399–7422, https://doi.org/10.1016/j.ijsolstr.2004.06.038.
[21] S. Gonella, M. Ruzzene, Homogenization and equivalent in-plane properties of two-dimensional periodic lattices, Int. J. Solids Struct. 45 (10) (2008) 2897–2915, https://doi.org/10.1016/j.ijsolstr.2008.01.002.
[22] W. Burton, A. Noor, Assessment of continuum models for sandwich panel honeycomb cores, Comput. Methods Appl. Mech. Eng. 145 (3) (1997) 341–360, https://doi.org/10.1016/S0045-7825(96)01196-6.
[23] S. Balawi, J. Abot, The effect of honeycomb relative density on its effective in-plane elastic moduli: an experimental study, Compos. Struct. 84 (4) (2008) 293–299, https://doi.org/10.1016/j.compstruct.2007.08.009.
[24] A. Karakoç, J. Freund, Experimental studies on mechanical properties of cellular structures using nomex® honeycomb cores, Compos. Struct. 94 (6) (2012) 2017–2024, https://doi.org/10.1016/j.compstruct.2012.01.024.
[25] C.W. Schwingshackl, G.S. Aglietti, P.R. Cunningham, Determination of honeycomb material properties: existing theories and an alternative dynamic approach, J. Aerosp. Eng. 19 (3) (2006) 177–183, https://doi.org/10.1061/(ASCE)0893-1321(2006)19:3(177).
[26] M.J. Silva, L.J. Gibson, The effects of non-periodic microstructure and defects on the compressive strength of two-dimensional cellular solids, Int. J. Mech. Sci. 39 (5) (1997) 549–563, https://doi.org/10.1016/S0020-7403(96)00065-3.
[27] A. Simone, L. Gibson, Aluminum foams produced by liquid-state processes, Acta Mater. 46 (9) (1998) 3109–3123, https://doi.org/10.1016/S1359-6454(98)00017-2.
[28] A. Simone, L. Gibson, Effects of solid distribution on the stiffness and strength of metallic foams, Acta Mater. 46 (6) (1998) 2139–2150, https://doi.org/10.1016/S1359-6454(97)00421-7.
[29] H. Zhu, J. Knott, N. Mills, Analysis of the elastic properties of open-cell foams with tetrakaidecahedral cells, J. Mech. Phys. Solids 45 (3) (1997) 319–343, https://doi.org/10.1016/S0022-5096(96)00090-7.
[30] J. Storm, M. Abendroth, D. Zhang, M. Kuna, Geometry dependent effective elastic properties of open-cell foams based on Kelvin cell models**, Adv. Eng. Mater. 15 (12) (2013) 1292–1298, https://doi.org/10.1002/adem.201300141.

[31] A. Zargarian, M. Esfahanian, J. Kadkhodapour, S. Ziaei-Rad, Effect of solid distribution on elastic properties of open-cell cellular solids using numerical and experimental methods, J. Mech. Behav. Biomed. Mater. 37 (2014) 264–273, https://doi.org/10.1016/j.jmbbm.2014.05.018.
[32] C.-H. Chuang, J.-S. Huang, Effects of solid distribution on the elastic buckling of honeycombs, Int. J. Mech. Sci. 44 (7) (2002) 1429–1443, https://doi.org/10.1016/S0020-7403(02)00039-5.
[33] M.-Y. Yang, J.-S. Huang, Elastic buckling of regular hexagonal honeycombs with Plateau borders under biaxial compression, Compos. Struct. 71 (2) (2005) 229–237, https://doi.org/10.1016/j.compstruct.2004.10.014.
[34] L. Zhang, B. Liu, Y. Gu, X.H. Xu, Modelling and characterization of mechanical properties of optimized honeycomb structure, Int. J. Mech. Mater. Des. 16 (2020) 155–166, https://doi.org/10.1007/s10999-019-09462-0.
[35] Ting-Chun Lin, Mei-Yi Yang, Jong-Shin Huang, Effects of solid distribution on the out-of-plane elastic properties of hexagonal honeycombs, Compos. Struct. 100 (2013) 436–442, https://doi.org/10.1016/j.compstruct.2013.01.007.
[36] S. Li, Boundary conditions for unit cells from periodic microstructures and their implications, Compos. Sci. Technol. 68 (9) (2008) 1962–1974, https://doi.org/10.1016/j.compscitech.2007.03.035.
[37] S. Li, On the unit cell for micromechanical analysis of fibre-reinforced composites, Proc. R. Soc. Lond., Ser. A, Math. Phys. Eng. Sci. 455 (1983) (1999) 815–838, https://doi.org/10.1098/rspa.1999.0336.
[38] S. Li, General unit cells for micromechanical analyses of unidirectional composites, Composites, Part A, Appl. Sci. Manuf. 32 (6) (2001) 815–826, https://doi.org/10.1016/S1359-835X(00)00182-2.
[39] I. Kuszczak, F. Azam, M. Bessa, P. Tan, F. Bosi, Bayesian optimisation of hexagonal honeycomb metamaterial, Extrem. Mech. Lett. 64 (2023) 102078, https://doi.org/10.1016/j.eml.2023.102078.
[40] C. Riccio, M. Civera, O. Grimaldo Ruiz, P. Pedullà, M. Rodriguez Reinoso, G. Tommasi, M. Vollaro, V. Burgio, C. Surace, Effects of curing on photosensitive resins in sla additive manufacturing, Appl. Mech. 2 (4) (2021) 942–955, https://doi.org/10.3390/applmech2040055.
[41] P. Onck, E. Andrews, L. Gibson, Size effects in ductile cellular solids. Part I: modeling, Int. J. Mech. Sci. 43 (3) (2001) 681–699, https://doi.org/10.1016/S0020-7403(00)00042-4.
[42] C. Chen, T. Lu, N. Fleck, Effect of imperfections on the yielding of two-dimensional foams, J. Mech. Phys. Solids 47 (11) (1999) 2235–2272, https://doi.org/10.1016/S0022-5096(99)00030-7.
[43] C.-H. Chuang, J.-S. Huang, Elastic moduli and plastic collapse strength of hexagonal honeycombs with Plateau borders, Int. J. Mech. Sci. 44 (9) (2002) 1827–1844, https://doi.org/10.1016/S0020-7403(02)00139-X.
[44] S. Malek, L. Gibson, Effective elastic properties of periodic hexagonal honeycombs, Mech. Mater. 91 (2015) 226–240, https://doi.org/10.1016/j.mechmat.2015.07.008.
[45] X. Hou, F. Xie, T. Sheng, Z. Deng, A new honeycomb design strategy for favoring pattern transformation under uniaxial loading, Int. J. Solids Struct. 295 (2024) 112812, https://doi.org/10.1016/j.ijsolstr.2024.112812.